Available online at www.sciencedirect.com
ScienceDirect
Journal of Catalysis 251 (2007) 223–232
JOURNAL OF CATALYSIS
www.elsevier.com/locate/jcat

Development of Ni–Cu–Mg–Al catalysts for the synthesis of carbon nanofibers by catalytic decomposition of methane

L. Dussault [a], J.C. Dupin [a], C. Guimon [a], M. Monthioux [b], N. Latorre [c], T. Ubieto [c], E. Romeo [c], C. Royo [c], A. Monzón [c,*]

[a] *Institut Pluridisciplinaire de Recherche sur l'Environnement et les Matériaux, Equipe de Chimie, Physique (IPREM-ECP), UMR #5254 CNRS, 2 Av. P. Angot, F-64053 Pau Cedex 9, France*
[b] *CEMES, UPR-8011 CNRS, B.P. 94347, 31055 Toulouse Cedex 4, France*
[c] *Department of Chemical and Environmental Engineering, Institute of Nanoscience of Aragon (INA), University of Zaragoza, 50009 Zaragoza, Spain*

Received 10 February 2007; revised 23 May 2007; accepted 16 June 2007

Available online 21 August 2007

Abstract

This work presents the kinetics and characterization results of Ni–Cu–Mg–Al catalysts used for the synthesis of carbon nanofibers (CNFs) by catalytic methane decomposition (CCVD). Ni–Cu–Mg–Al-based lamellar double hydroxides (LDHs) were synthesized by the coprecipitation method using either a regular maturation stage or a colloid mill process. After calcination at 1073 K and reduction at 1023 K, the formation of alloyed Ni–Cu nanoparticles over a mixed $MgO–MgAl_2O_4–NiAl_2O_4$ support was observed. The kinetic study of CNF synthesis by CCVD of methane was carried out in a thermobalance operated as a differential reactor. Small proportions of Cu ($\leqslant 10$ wt%) were found to improve the activity and mainly the stability over time of Ni–Mg–Al catalysts. On the other hand, large proportions of Cu dramatically decrease the activity of the catalysts in terms of CNF yield. The catalysts were able to produce high-quality CNFs with a graphitic or turbostratic structure. The size of metal particles and the diameter of carbon filaments obtained depend on the catalyst composition (i.e., Ni:Cu ratio). The application of a kinetic model based on the growing mechanism of CNFs allows us to determine the influence of the operating conditions on the kinetic parameters.

Keywords: Catalytic methane decomposition; Carbon nanofiber; Ni–Cu–Mg–Al catalysts; LDH precursors; Kinetic modeling

1. Introduction

Over the last decade, carbonaceous nanomaterials have received considerable attention due to their physical and chemical properties and their potential industrial applications. This is particularly the case for carbon nanofibers (CNFs) (see, e.g., the reviews by De Jong and Geus [1] and Serp et al. [2]), which can be used as catalyst supports [2–7], electrodes for fuel cells [8] and lithium ion batteries [9], adsorbents [10,11], polymer additives [12], and possibly gas storage materials [13–15].

CNFs usually are obtained by catalytic chemical vapor deposition (CCVD) from the decomposition of gaseous hydrocarbons (e.g., methane) on third-transition metal particles. For a long time, the deposition over catalysts of carbon in various forms, including nanosized filaments (i.e., CNFs), had to be avoided because of their deactivation effects in catalytic dehydrogenation reactions and the cracking of hydrocarbons [16–21]. The overall mechanism of CNF growth over metallic particles is now well established [1]. It consists of several steps: (i) Methane is cracked on the metal surface; (ii) carbon atoms, which can form subsurface carbides, dissolve and diffuse through the bulk of the solid or through quasi-liquid metal particles; (iii) due to the cooling down of the particles that lower the carbon solubility or due to oversaturation, carbon is then expelled and precipitates as more or less perfect polyaromatic layers (graphenes). This continuous process explains why the metal particles are most often located at the tips of the CNFs. CNF diameter can range from 2 to 500 nm [1,21] and depends mainly on the metal particle size. Two main types of carbon filaments can be obtained: hollow, thereby forming nanotubes in which graphenes are displayed parallel (i.e., concentric texture)

* Corresponding author.
E-mail address: amonzon@unizar.es (A. Monzón).

0021-9517/$ – see front matter
doi:10.1016/j.jcat.2007.06.022

or oblique (i.e., herringbone texture) to the filament axis, and genuine nanofibers in which graphenes are displayed oblique (herringbone texture) or perpendicular (platelet texture) to the fiber axis while leaving no inner cavity. Both CNF type and size depend on the metal particle features (i.e., size, morphology, composition), the carbon source, and the reaction conditions.

Among the different metals commonly used in CNF and H_2 production, Ni-based supported catalysts are of special interest because they show good activity at relatively moderate temperatures [18,22–26]. Indeed, the decomposition temperature of methane (870–970 K) with these catalysts is about 300 K lower than that with Fe-based catalysts. The most frequently used supports are silica, alumina, and magnesia. Given the beneficial effect of using such alloys as Fe–Mo, associating another metal, such as Cu [27–31], to Ni has been proposed to increase the activity. Li et al. [29] have thus demonstrated that a small proportion of Cu promotes the activity of Ni/Al_2O_3. However, Ni-based catalysts with high nickel content tend to deactivate themselves relatively quickly by sintering and formation of encapsulating polyaromatic carbon shells. Adding Mg to Ni–Al catalysts obtained by coprecipitation improves the properties of these solids [32]. Ni–Mg–Al catalysts are more resistant to deactivation than Ni–Al catalysts, because the formation of a spinel phase of $MgAl_2O_4$ provides stability to the Ni particles, avoiding sintering and consequent deactivation. Moreover, Ni–Mg–Al catalysts have a greater specific surface area, and thus a higher reactivity per gram of catalyst, than Ni–Al catalysts.

Taking these properties into account, we prepared Ni–Cu–Mg–Al mixed oxides from lamellar double hydroxides (LDHs), also known as Feiknecht or hydrotalcite-like compounds. These precursors belong to a large class of anionic clay minerals formed by brucite-like $[Mg(OH)_2]$ sheets in which the octahedral divalent magnesium is partially isomorphously substituted by divalent (e.g., Ni, Cu) and trivalent (e.g., Al) cations. The positive charges resulting from the trivalent cations are compensated by anions (e.g., CO_3^{2-}, NO_3^{2-}, Cl^-) located in the interlayer space together with water molecules [33]. In these compounds, the metallic atoms have a uniform distribution, so that calcination between 673 and 1073 K transforms the hydroxides into well-mixed oxides. This maximizes the intermetallic interactions, which favors the doping effect of Cu [29] and the formation of Ni–Cu alloy. Moreover, the irreducible domains (Al_2O_3, MgO, nickel, and magnesium aluminates) act as supports, minimizing the sintering effect during calcination and prereduction and inducing a decrease in metal particle size.

To improve the stability of the catalysts and minimize their deactivation with time, we have used smaller proportions of the reducible metals than those reported in the literature. We prepared the LDH precursors of molecular formula $(Ni_{1-x}Cu_xMgAl)(OH)_7(CO_3^{2-})_{0.5}$, with $0 \leqslant x \leqslant 1$, using two different methods: the conventional coprecipitation process and, with the aim of tuning the particle size control, the colloid mill coprecipitation method. Here we report the results from the characterization and catalyst activity of $(NiO)_{1-x}(CuO)_xMgO(Al_2O_3)_{0.5}$ catalysts obtained from the LDH precursors as a function of catalyst composition and preparation procedure. The results include a kinetic study of the influence of the operating conditions on the rate of CNF growth. We have presented a detailed CNF characterization and a discussion of the relationship between catalyst characteristics and nanofiber type in another paper [34]. In what follows, for the sake of simplicity, we designate the catalysts as $Ni_{1-x}Cu_xMgAl$ (e.g., $Ni_{0.8}Cu_{0.2}MgAl$ for $x = 0.2$).

2. Experimental

2.1. Catalytic precursors

We first prepared two aqueous solutions, one containing various amounts of $Mg(NO_3)_2{\cdot}6H_2O$, $Al(NO_3)_3{\cdot}9H_2O$, $Cu(NO_3)_2{\cdot}3H_2O$, and $Ni(NO_3)_2{\cdot}6H_2O$, and another containing NaOH (to maintain the pH constant at 9.5 ± 0.2) and a slight excess of Na_2CO_3. LDH materials with various Ni/Cu/Mg/Al proportions (given in Table 1) were then prepared from the latter solutions using two different methods, the regular coprecipitation method [35] and a coprecipitation route using a colloid mill [36].

In the regular coprecipitation route, the two solutions were simultaneously added dropwise to a vessel containing stirred, deionized water, with the pH of the mixture maintained at 9.5. The mixing process was carried out at room temperature. The resulting slurry was removed from the vessel and kept as a suspension at 348 K for 15 h under stirring. The precipitate was then filtered, washed with deionized water, and dried overnight at 353 K. For the colloid mill method [36], the two solutions were simultaneously added in a colloid mill rotating at 3000 rpm and mixed for 5 min. The resulting slurry was removed from the colloid mill and kept as a suspension at 348 K

Table 1
Atomic ratios of LDH precursors $(Ni_{1-x}Cu_xMgAl)(OH)_7(CO_3^{2-})_{0.5}$ (ICP-AES) and BET surface area values before (393 K) and after (1073 K) calcination

Nominal value of x	Mg/Al (±0.05)	Ni/Cu (±0.05)	Ni/Al (±0.05)	Cu/Al (±0.05)	393 K ($m^2\,g^{-1}$)	1073 K ($m^2\,g^{-1}$)
$x = 0$	1	/	1	/	87	159
$x = 0.05$	1	17.2	0.9	0.05	162	177
$x = 0.1$	1	8.15	0.9	0.1	147	164
$x = 0.2$	0.75	4	0.8	0.2	228	159
$x = 0.5$	1	1	0.5	0.5	142	150
$x = 0.8$	0.9	0.25	0.2	0.8	130	70
$x = 1$	0.75	/	/	1	84	65

for 15 h under stirring. The precipitate was then filtered, washed with deionized water, and dried overnight at 353 K. The composition of the resulting LDHs is provided in Table 1.

2.2. Characterization

The X-ray diffraction (XRD) patterns were recorded with an INEL diffractometer using a curved position-sensitive detector (INEL CPS 120) calibrated with $Na_2Ca_3Al_2F_{14}$ as the standard. The monochromatic radiation applied was CuK_α (1.5406 Å) from a long fine-focus Cu tube operating at 40 kV and 20 mA. Scans were performed over 2θ angles ranging from 10 to 90°. The powder diffraction standards (JCPDS) were used for peak assignment.

The elemental composition of the samples was determined by AES-ICP in a Thermo-Electron model 3580 instrument with a H_2SO_4/HNO_3 solution at 523 K. Surface areas were determined by the BET method from the adsorption of nitrogen at 77 K using a Micromeritics sorptometer. The samples (0.05 g) were pretreated at 393 K overnight under vacuum (ca. 16 h, 10^{-5} mbar) to remove moisture before analysis.

Thermogravimetric experiments (on ca. 10 mg) were carried out with a TGA model 2950 coupled with a TA Instruments mass spectrometer from 303 to 1123 K (5 K min^{-1}) under air flow.

Before obtaining the temperature-programmed reduction (TPR) measurements, the precursors (100 mg) were calcined at 1073 K under argon flow with a heating rate of 5 K min^{-1} and plateaus at 453 K (1 h), 573 K (1 h), and 1073 K (11 h). TPR experiments were then carried out at a 4 K min^{-1} ramp from 303 to 1173 K in a quartz reactor with a flow system (GIRA, X-sorb model) equipped with a thermal conductivity detector. A hydrogen–argon mixture (5–95%) was used as the reducing atmosphere with a flow rate of 20 ml N min^{-1}.

The XPS analyses were carried out with a Kratos spectrometer (model Axis Ultra) with focused monochromatic AlK_α radiation (1486.6 eV) under a residual pressure of 10^{-7} Pa. To prevent exposure of the samples to air between the calcination step, the reduction step, and analysis, the XPS spectrometer was directly coupled to a glove box. The hemispherical analyzer functioned with a constant pass energy of 40 eV for high-resolution spectra. The area of the samples analyzed was 300×700 μm^2. Charge neutralization was used for all measurements to compensate for the charge effects. The binding energy scale was calibrated using the Al2p peak at 74.1 eV (corresponding to Al_2O_3) for calcined samples. The fitting peaks of the experimental curves were calculated using a combination of Gaussian (70%) and Lorentzian (30%) functions with a nonlinear Shirley-type background. The XPS quantitative analyses were performed with the appropriate Scofield factors [37].

Dynamic light scattering (DLS) was used on 1 mg ml^{-1} of suspended catalyst materials in glycol ethylene (1 mol l^{-1}) to measure the average particle size. The apparatus consisted of a power laser Spectra-Physics Stabilite 2017 (wavelength = 514.5 nm, power = 0.1–2 W) and a Sematech photogoniodiffusiometer.

The Raman spectra were obtained using a Jobin Yvon T64000 confocal spectrophotometer in air and at room temperature. Spectra were acquired with a 514.5 nm Ar^+ ion laser as an excitation source.

Scanning electron microscopy (SEM) studies were carried out with a LEO 1530 Vp microscope under ultra-high vacuum, with voltages of 20–30 kV, an in-lens detector and a 30-μm aperture.

2.3. Synthesis of CNFs

LDH materials from both routes (regular and colloid mill methods) were calcined at 1073 K under a nitrogen flow after a 5 K min^{-1} ramp, with three plateaus at 453 K (1 h), 573 K (1 h), and 1073 K (11 h), resulting in catalytic materials of various compositions. Approximately 100 mg of each catalyst was then placed in the quartz basket of a thermal balance (CI Electronics) operated as a differential reactor. Catalyst reduction was performed in situ at 1023 K for 2 h using a H_2 (40%)/N_2 mixture, at a flow of 250 Nml min^{-1}. Reaction conditions were temperature, 848–973 K; total flow rate, 750 Nml min^{-1}; and feed composition (%CH_4/%H_2/%N_2), 2.5/0/97.5–10/10/80. After reaction, the reactor was cooled down to room temperature in a N_2 atmosphere.

3. Results and discussion

3.1. From LDH precursors to mixed oxides

The elemental analysis (ICP-AES) (Table 1) found that the composition of the LDH precursors was very close to that of the reactive mixture, particularly regarding reducible metals (Ni and Cu). Only samples with $x = 1$ and 0.2 showed a slight loss of magnesium (Mg/Al = 0.75 instead of 1).

To follow the transformation of the hydroxide precursors into mixed oxides, diffractograms were obtained before and after calcination at 1073 K. All of the precursors showed a hydrotalcite-like structure with a good crystallinity regardless of the coprecipitation route (not shown here). At 1073 K, the structure changed drastically. Fig. 1a shows an example ($Ni_{0.9}Cu_{0.1}$MgAl, i.e., $x = 0.1$) of the diffractogram after calcination at 1073 K. As expected, this diffractogram shows the formation of aluminates, $MgAl_2O_4$ (JCPDS file no. 75-1801), $NiAl_2O_4$ (JCPDS file no. 78-1601) with spinel-like structure (JCPDS file no. 78-0430), NiO (JCPDS file no. 78-0643), and CuO (JCPDS file no. 80-1916). By TGA and XPS analysis (not shown here), it was observed that the transformation of LDHs into mixed oxides was accompanied by the loss of carbonate ions and water. If at 723 K, about 30% of carbonates remain [38], then XPS analysis indicates that practically no carbonate remains after calcination at 1073 K. The specific surface areas of the mixed oxides obtained at 1073 K were relatively close to those of the LDH precursors (Table 1). It appears that these areas increased with the nickel proportion and that a small proportion of Cu improved them slightly (comparison between $x = 0$ and 0.05).

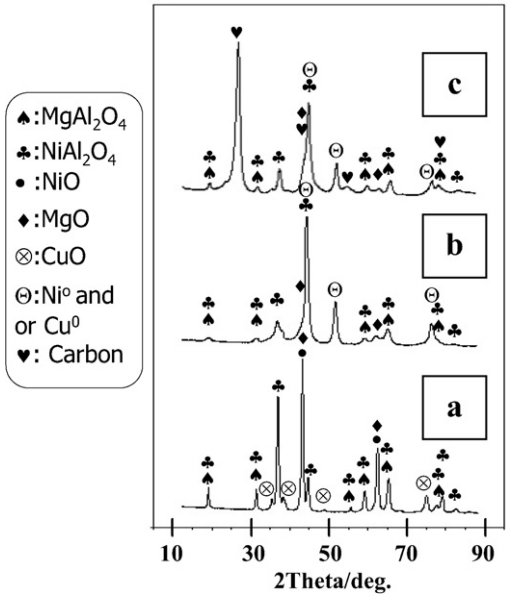

Fig. 1. XRD patterns of $Ni_{0.9}Cu_{0.1}MgAl$ after calcination at 1073 K (a), then reduction at 1023 K (b) and after reaction (c).

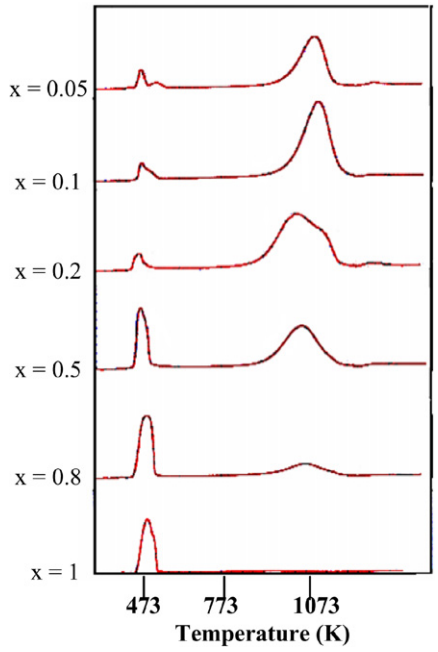

Fig. 2. TPR (300–1173 K) of the mixed oxides $(NiO)_{1-x}(CuO)_xMgO$-$(Al_2O_3)_{0.5}$ obtained by calcination of $(Ni_{1-x}Cu_xMgAl)(OH)_7(CO_3^{2-})_{0.5}$ LDHs at 1073 K.

3.2. Characterization of reduced mixed oxides

To be active in the production of CNFs, the catalysts must be in reduced state. The reducibility of the catalysts was studied by TPR. The TPR curves (Fig. 2) show two reduction regions, the first at 443–503 K and the second at 973–1173 K.

The first region corresponds to the reduction of copper ($Cu^{II} \rightarrow Cu^0$). The one-step reduction of malachite is associated with a single, quite sharp peak with a maximum at 503 K [38]. Fierro et al. [39] showed that the reduction temperature

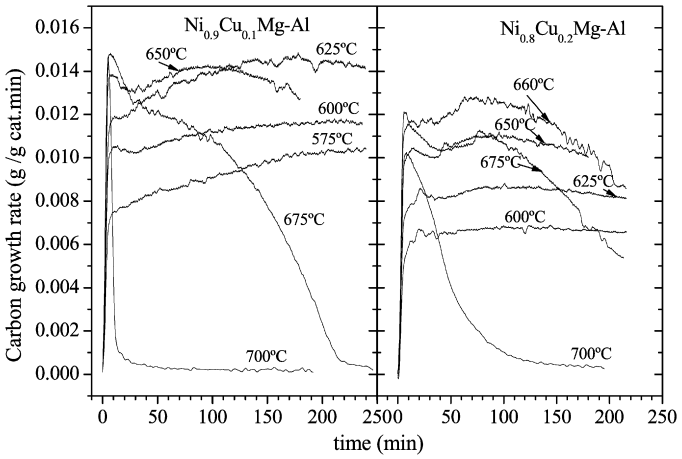

Fig. 3. Evolution with time of the carbon growth rate for the $Ni_{0.8}Cu_{0.2}MgAl$ and $Ni_{0.9}Cu_{0.1}MgAl$ catalysts. Influence of operating temperature.

and the peak width tend to decrease with decreasing particle size. The curves of H_2 consumption, TPR, reported in Fig. 2 indicate an evolution with a Cu content similar to that of Cu–Zn supported catalysts [39]. The high-Cu content samples (x between 1 and 0.5) presented a single band with a FWHM of about 50 K. For the low-Cu content samples, a double peak appeared with smaller widths (∼20 K), which indicates smaller particle sizes. This is in agreement with a better dispersion of Cu cations over the support, as noted by Wang et al. [31], and can be related to the greater BET areas for the smallest values of x. The small CuO particles could have more interaction with the other metals, particularly Ni, which can form Ni–Cu alloy after reduction. It is indeed known that Ni and Cu easily form alloys over a wide composition range [30,40]. The absence of a peak toward 770 K shows that $CuAl_2O_4$ was not formed [41].

The second region at 970–1170 K is associated with the reduction of the nickel ($Ni^{II} \rightarrow Ni^0$), because magnesium and aluminum oxides do not reduce below 1170 K. Such temperatures are much higher than those for pure NiO, which is reduced at 600–700 K [42]. This demonstrates a strong interaction of the nickel with the neighboring metals [20]. As with copper, the broad band can be decomposed into two components centered at 1020 and 1120 K. The former corresponds to NiO particles in intimate contact with the support, whereas the latter can be associated with the reduction of nickel aluminate [43–46] observed in the XRD patterns (Fig. 1) and maybe in part with small NiO particles buried in the $MgAl_2O_4$ matrix. The presence of these different types of nickel was confirmed by XPS analysis of the samples reduced at 1023 K. In samples with high Ni content, when the copper was totally reduced (binding energy $Cu2p_{3/2}$ at 932.5 eV and Auger band at 919 eV), the $Ni2p_{3/2}$ band indicated the presence of about 30% of Ni^0 (BE at 852.5 eV) and 70% of Ni^{II} (BE at 855 eV), nonreducible at this temperature.

According to TPR and confirmed by XRD and XPS, it seems that the NiO/$NiAl_2O_4$ ratio decreased with increasing Ni content, which may be related to a stabilizing interaction between the nickel and copper oxides. However, the total NiO content seemed to reach its maximum for a composition with a value of

Table 2
Average size and size distribution obtained from light scattering of particles of $Ni_{0.8}Cu_{0.2}Mg.Al$ ($x = 0.2$) and $Ni_{0.9}Cu_{0.1}Mg.Al$ ($x = 0.1$) prepared by conventional method and with colloid mill at various steps of the preparation process

x	Preparation method	As-synthesized		Calcined (1073 K) average size (nm)	Calcined (1073 K) reduced (1023 K) average size (nm)
		Average size (nm)	Size range (nm)		
0.2	Conventional coprecipitation	155	20–1000	215	175
0.2	Colloid mill	95	25–500	160	150
0.1	Conventional coprecipitation	100	25–400	140	130
0.1	Colloid mill	100	25–300	135	140

x of 0.1–0.2, consistent with the activity of these catalysts (vide infra, Section 3.4).

To summarize, after prereduction at 1023 K, the above results demonstrate that the catalysts are composed of Cu^0, Ni^0 (probably as a Ni–Cu alloy), MgO, $NiAl_2O_4$, and $MgAl_2O_4$.

3.3. Particle size

The particle size of the catalysts (metals and support) and their distribution depend on the catalyst composition and preparation method [47–50]. In parallel to the common coprecipitation method, LDHs can be prepared using a colloid mill (see Section 2), which allows very rapid mixing and nucleation, followed by a separate aging step. This method, first proposed by Zhao et al. [36], gives smaller LDH crystals with a narrow size distribution (Table 2).

The size range and related average values tended toward lower values when using the colloid mill method instead of the conventional method and a composition of $x = 0.1$ instead of 0.2. This is quite obvious right after synthesis, where size distributions were 20–1000 nm for $x = 0.2$ under the coprecipitation method (average, 155 nm), 25–500 nm for $x = 0.2$ using the colloid mill (average, 95 nm), 25–400 nm for $x = 0.1$ with the coprecipitation method (average, 100 nm), and 25–300 nm for $x = 0.1$ using the colloid mill (average, 100 nm). After calcination and prereduction, however, the values were close (130–175 nm), regardless of the conditions.

3.4. Catalytic activity and CNF growth

Copper is almost inactive for this reaction and has a dilution effect on the active sites. Thus, an excessive Cu content dramatically decreases the carbon yield [29,51]. Nevertheless, the presence of Cu in the catalyst composition affects carbon diffusion and reaction rates [29,52], and thus promotes catalytic activity when it is incorporated in small quantities. The maximum carbon yield is reached for Cu content ranging between 3 wt% [27] and 15 wt% [28]. In agreement with these results, our catalysts with $x \geqslant 0.5$ showed very low activity [53]. The maximal yield was obtained with the $Ni_{0.9}Cu_{0.1}MgAl$ and $Ni_{0.8}Cu_{0.2}MgAl$ catalysts (i.e., 3.8 and 7.6 wt% Cu, respectively). These catalysts showed higher resistance against deactivation than $Ni.MgAl_2O_4$ catalyst because Cu favors hydrogen mobility, inhibiting the formation of encapsulating coke [52]. Moreover, we found that the synthesis method did not affect the catalyst activity and stability.

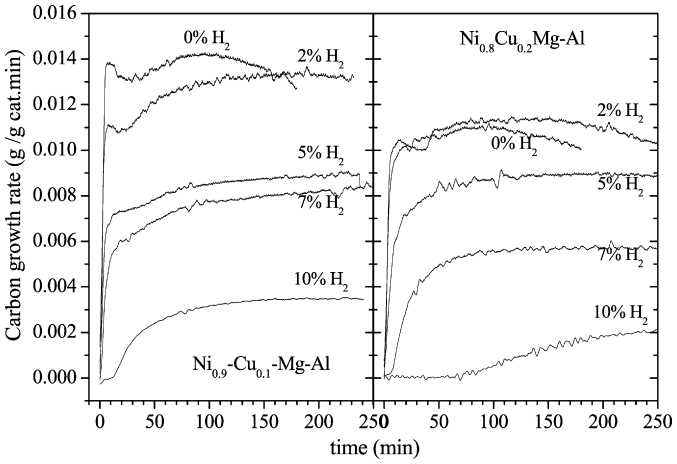

Fig. 4. Evolution with time of the carbon growth rate for the $Ni_{0.8}Cu_{0.2}MgAl$ and $Ni_{0.9}Cu_{0.1}MgAl$ catalysts. Influence of hydrogen partial pressure.

The operating temperature has a significant influence on the yield (Fig. 3). In our case, the optimal temperature was close to 923 K, slightly lower than that determined with other similar systems, such as Ni–Cu–Mg [31] (around 973 K). The feed composition in these experiments was 5% CH_4/95% N_2. An increase in the reaction temperature heightened the kinetics of methane decomposition and deactivation reactions. At low reaction temperatures, the carbon formation rate was low, but deactivation was not observed for the reaction time. The deactivation rate was faster at higher reaction temperatures. When deactivation occurred, the carbon formation rate curves showed an initial period of rapid growth until a maximum was reached, followed by a decrease in rate until a residual constant value was reached. During the period of activity decay, the deactivation rate exceeded the filament formation rate; consequently, the catalysts showed an optimal operating temperature at the maximum carbon content.

The $Ni_{0.9}Cu_{0.1}MgAl$ catalyst showed a higher carbon formation rate than $Ni_{0.8}Cu_{0.2}MgAl$ at the temperatures tested. Furthermore, $Ni_{0.9}Cu_{0.1}MgAl$ exhibited greater sensitivity to the reaction temperature, being almost inactive at 700 °C. This catalyst had good yields in an optimum range of operating temperatures and was very active and stable.

Fig. 4 shows the effect of P_{H_2} at a constant P_{CH_4} (0.05 atm) and operating temperature (650 °C). Hydrogen prevents the formation of encapsulating coke, and consequently the formation of carbon filaments is not hindered by this coke [5]. This fact explains why deactivation was avoided during the CNFs syn-

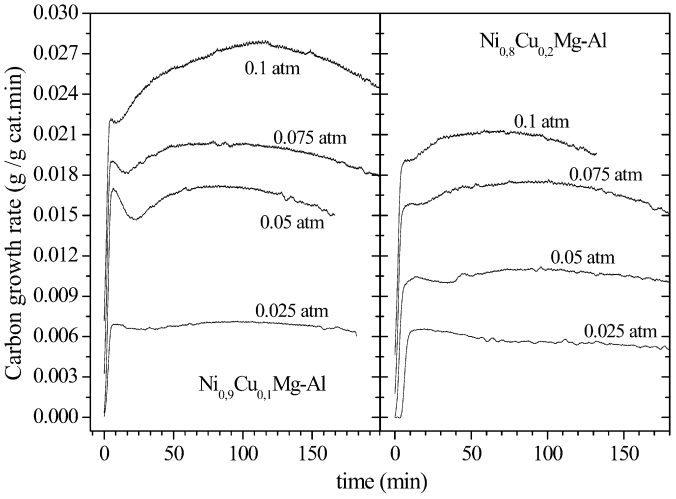

Fig. 5. Evolution with time of the carbon growth rate for the $Ni_{0.8}Cu_{0.2}MgAl$ and $Ni_{0.9}Cu_{0.1}MgAl$ catalysts. Influence of methane partial pressure.

thesis when the P_{H_2} was approximately 0.02 atm. However, at high P_{H_2}, the greater competition between H_2 and CH_4 for the metallic surface sites caused a diminution in the carbon formation rate.

The effect of P_{CH_4} on the carbon formation rate is characterized in Fig. 5. The operating temperature in these experiments was 650 °C ($P_{H_2} = 0$ atm). An augmentation of P_{CH_4} increased the carbon formation rate because higher methane concentrations in the gas phase led to a boost in the diffusion–precipitation process through the Ni crystallites. Moreover, an increase in the deactivation rate was not observed for the reaction time. As in the previous studies, the $Ni_{0.9}Cu_{0.1}MgAl$ catalyst showed greater yields than $Ni_{0.8}Cu_{0.2}MgAl$, with higher carbon contents and carbon formation rates.

With the aim of quantifying the influence of the operating conditions on the amount and rate of formation of the NCM, we developed a kinetic model for carbon growth during catalytic hydrocarbon decomposition [54–56]. The mathematical description of this kinetic model takes into account the main steps of carbon formation and accumulation over the catalyst: diffusion, nucleation, filament growth, and catalyst deactivation (Fig. 8). According to this model, the concentration of carbon accumulated over the catalyst, m_C ($g_C\,g_{cat}^{-1}$), and the carbon formation rate, r_C ($g_C\,g_{cat}^{-1}\,min^{-1}$), can be expressed as follows [54–57]:

$$m_C(t) = r_{C_0}\left[a_S t + \alpha_1 \cdot \left(1 - \exp(-\psi_G t)\right) - \alpha_2 \cdot \left(1 - \exp(-r_D t)\right)\right], \quad (1)$$

$$r_C(t) = r_{C_0}\left[a_S + \psi_G \alpha_1 \exp(-\psi_G t) - r_D \alpha_2 \exp(-r_D t)\right], \quad (2)$$

where α_1 and α_2 are given by

$$\alpha_1 = \frac{r_D(1 - a_S)}{\psi_G(r_D - \psi_G)}; \quad \alpha_2 = \frac{(r_D - \psi_G a_S)}{r_D(r_D - \psi_G)}. \quad (3)$$

The kinetic parameters of the model are as follows: r_{C_0} is the rate of carbon formation reached at steady state in the absence of catalyst deactivation; the units of this parameter are ($g_C\,g_{cat}^{-1}\,min^{-1}$); the term r_{C_0} is the product of the concentration

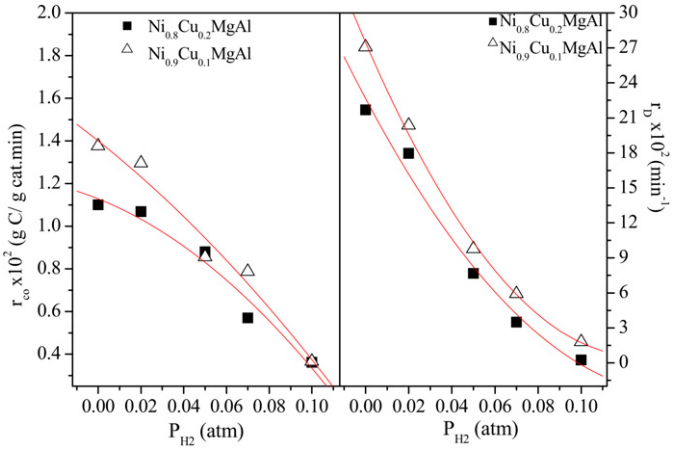

Fig. 6. Influence of hydrogen partial pressure on the kinetic parameters r_{C_0} and r_D.

Table 3
Apparent activation energies of the kinetic parameters

$Ni_{0.8}Cu_{0.2}MgAl$	ψ_d (min^{-1})	r_D (min^{-1})	r_{C_0} ($g_C\,g_{cat}^{-1}\,min^{-1}$)
E_a ($kJ\,mol^{-1}$)	164.6 ± 22.7	30.8 ± 0.5	66.7 ± 1.0
$Ni_{0.9}Cu_{0.1}MgAl$	ψ_d (min^{-1})	r_D (min^{-1})	r_{C_0} ($g_C\,g_{cat}^{-1}\,min^{-1}$)
E_a ($kJ\,mol^{-1}$)	–	111.3 ± 6.8	29.6 ± 2.3

of metallic active sites, C_{S_0}, by the carbon diffusion coefficient, k_C ($r_{C_0} = C_{S_0} \cdot k_C$) [54–56]; r_D is the intrinsic kinetic rate of methane decomposition over the metallic surface, min^{-1}; ψ_d is the deactivation kinetic function (in min^{-1}); and ψ_r is the regeneration kinetic function (in min^{-1}). These four parameters include the dependence on reaction temperature (i.e., apparent activation energies and preexponential factors), the atmospheric composition (kinetic orders), and the type and composition of the catalyst (metallic exposed area and intrinsic reactivity).

The term a_S represents the residual activity of the catalyst, which, according to the kinetic model, can be calculated as

$$a_S = (\psi_r/\psi_G); \quad \psi_G = \psi_d + \psi_r. \quad (4)$$

In the case where the catalyst suffers no deactivation, $\psi_d = \psi_r = 0$, and thus the residual activity of the catalyst is $a_S = 1$. In this case, Eqs. (1) and (2) are simplified to

$$m_C(t) = r_{C_0}\left[t - \frac{1}{r_D}\left(1 - \exp(-r_D t)\right)\right] \quad (5)$$

and

$$r_C(t) = r_{C_0}\left(1 - \exp(-r_D t)\right). \quad (6)$$

The foregoing expressions can be used directly to fit the experimental data in Figs. 4, 5, and 6 to obtain the dependence of the kinetic parameters with reaction temperature and partial pressures of H_2 and CH_4.

The values of the apparent activation energies of r_D, ψ_d, and r_{C_0}, calculated from the Arrhenius plots, are presented in Table 3. These values of E_a are similar to those commonly reported in the literature [54]. It can be seen that an increase in temperature caused increases in r_D, ψ_d, and r_{C_0},

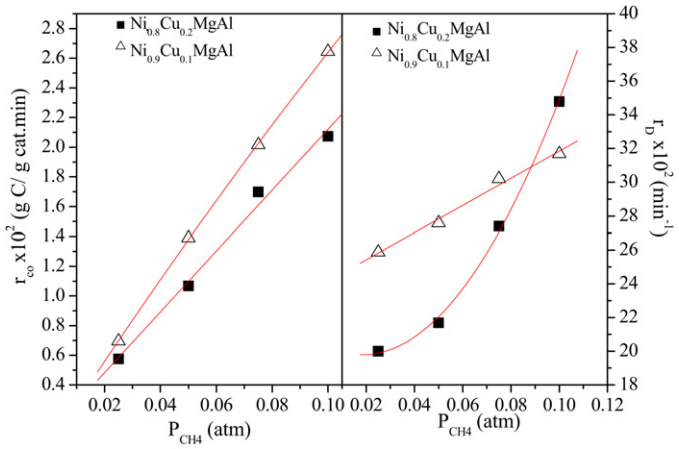

Fig. 7. Influence of methane partial pressure on the kinetic parameters r_{C_0} and r_D.

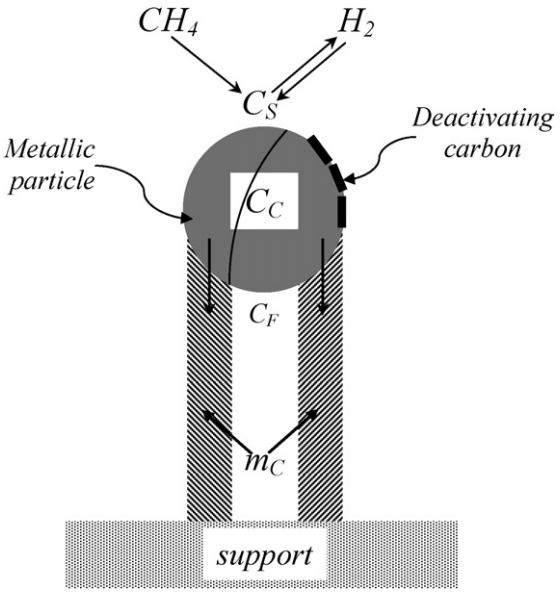

Fig. 8. Scheme with some parameters involved in the reaction kinetics of the nanocarbonaceous growth mechanism.

that is, increases in the methane decomposition rate, deactivation rate, and carbon diffusion through the metallic crystallites. Furthermore, the higher value of the apparent activation energies also demonstrates the higher activity and sensibility of the $Ni_{0.9}Cu_{0.1}MgAl$ catalyst with the reaction temperature.

Fig. 7 shows that both r_D and r_{C_0} decreased with P_{H_2}. The decrease in r_D was caused by the inhibitory effect of H_2 due to the competition with CH_4 for the metallic surface sites [19,57]. In addition, a higher H_2 concentration favored the reverse methane decomposition reaction, that is, carbon gasification. The decrease in r_{C_0} can be attributed to a reduction of effective sites caused by the inhibitory effect of hydrogen over the metallic surface. The values of both parameters were higher for the $Ni_{0.9}Cu_{0.1}MgAl$ catalyst, according to its higher activity. To clarify the effect of hydrogen on the parameters, we have assumed that r_D and r_{C_0} potentially depend on hydrogen pressure, according to

$$r_D = r_{D_{ref}} \left(\frac{P_{H_2}}{P_{H_2,ref}} \right)^{m_{D,H_2}} \left(\frac{P_{CH_4}}{P_{CH_4,ref}} \right)^{m_{D,CH_4}} \quad (7)$$

and

$$r_{C_0} = r_{C_{0,ref}} \left(\frac{P_{H_2}}{P_{H_2,ref}} \right)^{m_{C,H_2}} \left(\frac{P_{CH_4}}{P_{CH_4,ref}} \right)^{m_{C,CH_4}}. \quad (8)$$

Here P_{H_2} was normalized by dividing it by a reference pressure, usually the average value considering all of the experiments conducted. Therefore, $r_{C_{0,ref}}$ represents the preexponential parameter at this reference pressure. For our calculations, we used a H_2 reference pressure of 0.05 atm. The results, given in Table 4, indicate a strong negative dependence of r_D and r_{C_0} with respect to H_2. This negative dependence is a consequence of the competition effect of H_2 inhibiting the main reaction and causing an apparent decrease in activity but an increase in catalyst stability.

Finally, Fig. 7 shows that r_{C_0} followed an almost linear increase with the P_{CH_4}. This increase indicates a first-order dependence of this parameter on methane concentration, in agreement with previous studies [19,57]. As in the previous cases, the higher values of the parameters obtained for the $Ni_{0.9}Cu_{0.1}MgAl$ catalyst indicate the greater activity of this catalyst compared with $Ni_{0.8}Cu_{0.2}MgAl$ catalyst. As in the case of the study of influence of partial pressure of H_2, we also have assumed the same type of dependence for r_D and r_{C_0} with respect to partial pressure of methane as shown in Eqs. (7) and (8). In this case, the reference pressure of methane was 0.05 atm. Together with the apparent activation energies, these kinetics dates allow us to calculate reaction rates whatever the operating conditions within the range studied in this work.

3.5. Catalyst and carbon characterization after reaction

The XRD patterns of the reaction products (Fig. 1c) correspond exactly to the superposition of the diffractogram of the reduced catalyst (Fig. 1b) and that of polyaromatic carbon typical of graphene-based materials (002, 10, 004, and 11 reflections), such as CNFs and multiwall nanotubes. Thus, it seems

Table 4
Numerical values of potentially dependence on r_D and r_{C_0} parameters with hydrogen and methane pressure. Preexponential parameters and kinetic orders

	P_{H_2}		P_{CH_4}	
	$Ni_{0.8}Cu_{0.2}MgAl$	$Ni_{0.9}Cu_{0.1}MgAl$	$Ni_{0.8}Cu_{0.2}MgAl$	$Ni_{0.9}Cu_{0.1}MgAl$
r_{Dref}	0.035	0.071	0.266	0.293
m_D	−2.3	−1.4	0.38	0.15
r_{Cref}	0.007	0.008	0.010	0.020
m_C	−0.6	−0.7	0.95	0.96

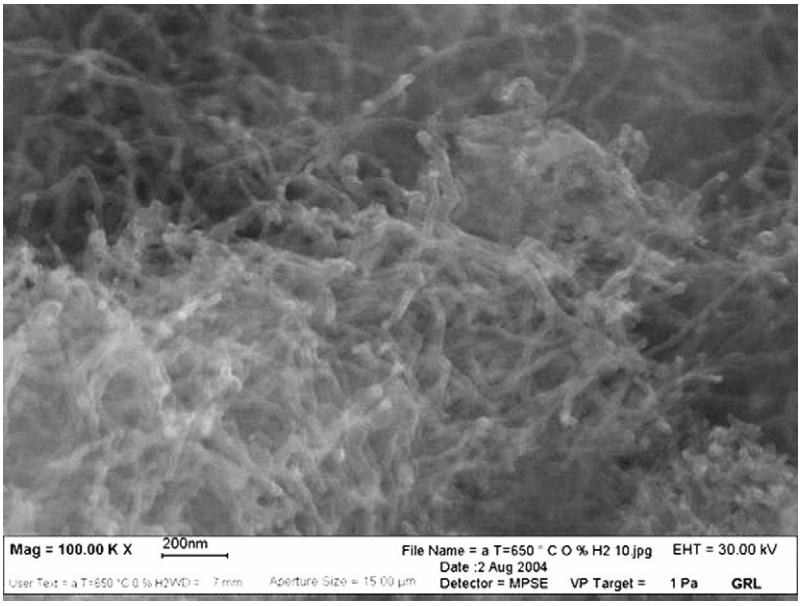

Fig. 9. SEM image of CNFs produced at 923 K over $Ni_{0.9}Cu_{0.1}MgAl$ catalyst. Feed composition: 5% CH_4; 95% N_2.

Table 5
Structural parameters of the CNFs from XRD: interlayer distance d_{002}, average size of coherently scattering domains along the normal to graphite layers (L_c) and in the layer plane (L_a)

	x			
	0.2	0.2	0.1	0.1
Preparation method	Conventional coprecipitation	Colloid mill	Conventional coprecipitation	Colloid mill
d_{002} (nm)	0.331	0.335	0.334	0.338
L_c (nm)	8.5	7.1	6.1	5.9
L_a (nm)	9.3	7.7	8.0	5.4

that the catalysts suffered no degradation during the first hours of reaction, and the sharpness of the related peaks indicates that the carbon thus formed had a relatively high nanotexture, related to relatively large, defect-free graphenes. This is confirmed by the structural parameters of the CNFs determined by XRD (Table 5), that is, the interlayer distance, d_{002}, and the average size of coherently scattering domains along the normal graphite layers (L_c) and in the layer plane (L_a). The average size decreased with decreasing x for both methods of catalyst synthesis used. The large sizes can be associated with a graphitic structure, whereas the smallest ones correspond to a turbostratic structure.

The filamentous morphology of the carbon products is illustrated by the SEM micrograph in Fig. 9. This figure clearly shows a dense population of entangled CNFs that form numerous mesopores (interstices between interlaced nanofibers). Thus these products contain both micropores and mesopores. The BET data for the products (about 165 $m^2\,g^{-1}$ with $Ni_{0.8}Cu_{0.2}MgAl$ and 130 $m^2\,g^{-1}$ with $Ni_{0.9}Cu_{0.1}MgAl$) seem to indicate a larger surface area for the former, which could correspond to a higher density of surface defects.

According to the above observations, the size of the catalyst particles, and consequently the diameter of the carbon filaments, decreased with decreasing Cu content and to a lesser extent when the colloid mill is used instead of the traditional mode of LDH preparation. The filaments generally had a diameter of 60–100 nm (with some thicker fibers up to 400 nm) for $Ni_{0.8}Cu_{0.2}MgAl$ (with the two preparation modes), 30–50 nm for $Ni_{0.9}Cu_{0.1}MgAl$ (traditional preparation mode), and 20–50 nm for $Ni_{0.9}\,Cu_{0.1}MgAl$ (use of colloid mill).

The graphene-based structure of the fibers observed in the XRD patterns (Fig. 1c) is confirmed by the Raman spectra and the XPS (C1s) analysis (not shown here). Raman spectroscopy is a powerful tool for studying carbon materials [58,59]. All of the Raman spectra in this study showed two intense bands, the first at 1580 cm^{-1} (E_{2g2}, usually called the G-band), assigned to the in-plane vibrations of carbon atoms in the hexagonal sheets, and the second at 1350 cm^{-1} (usually called the D-band), associated with disorder (lack of long-range translational symmetry) [60] and defects in the structure. Other bands were also associated with this disorder, including one at ∼1610 cm^{-1} (D′-mode), which became a shoulder of the G-band, and one at ∼2930 cm^{-1} (2D-mode). The frequency at about 2690 cm^{-1} also is associated with graphene perfection. The band at 1450–1550 cm^{-1}, characteristic of amorphous saturated carbon [61,62], was missing, indicating the very low content of this type of carbon in the products.

The ratios of the bands G and D (I_G/I_D: 0.51 and 0.77 for the products obtained over $Ni_{0.8}Cu_{0.2}MgAl_{0.5}$ and $Ni_{0.9}Cu_{0.1}MgAl_{0.5}$, respectively), at a reaction temperature of 923 K and a feed composition of 5% CH_4 and 95% N_2, indicate that the carbon obtained over the $Ni_{0.8}Cu_{0.2}MgAl_{0.5}$ catalyst had a more greatly disordered structure.

These observations agree with the findings of TG/DTG analyses (Fig. 10). The thermogravimetric curves showed a weight loss between 670 and 870 K. The differential curves indicated that the main part of the carbon loss was polyaromatic; the maximum rate was measured at about 850 K in all samples. The DTG peak exhibited a shoulder toward the low

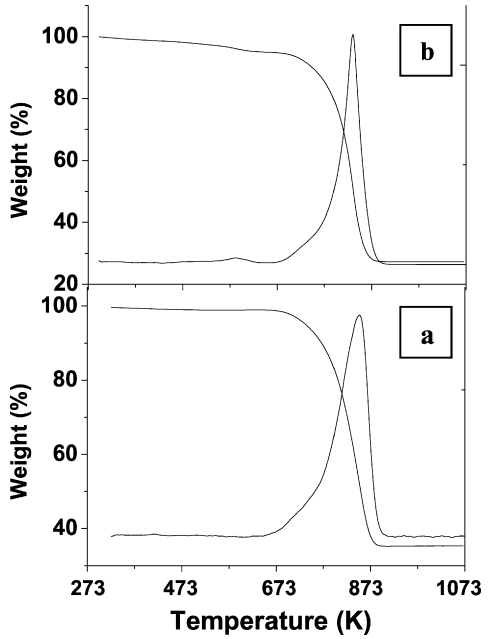

Fig. 10. TG/DTG analyses of carbon produced over $Ni_{0.8}Cu_{0.2}MgAl$ (a) and $Ni_{0.9}Cu_{0.1}MgAl$ (b) catalysts.

temperatures (∼720 K), which could correspond to amorphous carbon. This shoulder was slightly more intense and the width of the DTG peak at 850 K was greater for the product obtained over the $Ni_{0.8}Cu_{0.2}MgAl$ catalyst, possibly corresponding to a greater variation in size and perhaps also to slight differences in carbon filament texture or structure.

4. Conclusion

Numerous previous works have demonstrated that mixed or alloy catalysts have several advantages over single-metal catalysts for the production of nanostructured carbons. Consequently, we studied a series of catalysts ($Ni_{1-x}Cu_xMgAl$ with $0 < x < 1$) elaborated from LDHs. These precursors have the advantage of giving well-crystallized mixed oxides with a uniform distribution of the metallic elements. The physicochemical characteristics (e.g., reducibility, particle size) of these catalysts depend on their composition. The different techniques used (XRD, TPR, XPS) showed that the prereduced active catalysts were formed by particles of Cu^0 and Ni^0 (probably Ni–Cu alloy) on MgO, $NiAl_2O_4$, and $MgAl_2O_4$ supports. The shape (octahedral and cubo-octahedral) and the size of the catalyst particles varied with the composition, that is, with the value of x (decreasing as x decreased). The mode of synthesis of the LDH precursor also had a slight influence on particle size, especially on size distribution, which was narrower with the use of a colloid mill than with the conventional coprecipitation method.

The kinetic study of the carbon growth from the catalytic decomposition of methane indicates on the one hand good activity of the catalysts with low Cu content ($x \leqslant 0.2$) and on the other hand good stability over time of the $Ni_{1-x}Cu_xMgAl$ catalyst compared with the NiMgAl homologue. The kinetic model used allows discrimination of the influence of the operating conditions on the successive stages of CNF formation and growth. From this standpoint, the two best catalysts of the series studied were $Ni_{0.8}Cu_{0.2}MgAl$ (corresponding to 7.6 wt% of Cu) and especially $Ni_{0.9}Cu_{0.1}MgAl$ (corresponding to 3.8 wt% of Cu). According to the XRD and Raman spectra, the carbon products were typically polyaromatic CNFs with either a graphitic or a turbostratic structure. MEB images showed a mesoporosity due to the tangling of the nanofibers. The structure, texture, and growth mechanism of the CNFs will be discussed in a forthcoming paper [34].

Acknowledgments

Financial support was provided by the MEC, Madrid (project CTQ 2004-03973/PPQ). The authors thank J.P. Grenet and E. Pere (IPREM-ECP) for the Raman spectra and C. Quet (GRL-Arkema) for the MEB images.

References

[1] K.P. De Jong, J.W. Geus, Catal. Rev. Sci. Eng. 42 (2000) 481.
[2] P. Serp, M. Corrias, P. Kalk, Appl. Catal. A 253 (2003) 337.
[3] F. Salman, C. Park, R.T.K. Baker, Catal. Today 53 (1999) 385.
[4] C. Pham-Huu, N. Keller, G. Ehret, L.J. Charbonniere, R. Ziessel, M.J. Ledoux, J. Mol. Catal. A 170 (2001) 155.
[5] M.L. Toebes, J.H. Bitter, A.J. Van Dillen, K.P. de Jong, Catal. Today 76 (2002) 33.
[6] M.L. Toebes, F.F. Prinsloo, J.H. Bitter, A.J. Van-Dillen, K.P. de Jong, J. Catal. 214 (2003) 78.
[7] K. Takehira, T. Ohi, T. Shishido, T. Kawabata, K. Takaki, Appl. Catal. A 283 (2005) 137.
[8] C.A. Bessel, K. Lauberds, N.M. Rodriguez, R.T.K. Baker, J. Phys. Chem. B 105 (2001) 1115.
[9] S. Yoon, C. Park, H. Yang, Y. Korai, I. Mochida, R.T.K. Baker, N.M. Rodriguez, Carbon 42 (2004) 21.
[10] V.B. Fenelonov, L.B. Avdeeva, O.V. Goncharova, L.G. Okkel, P.A. Simonov, A.Y. Derevyankin, V.A. Likholobov, Stud. Surf. Sci. Catal. [Preparation of Catalysts VI] 91 (1995) 825.
[11] E.I. Bagrii, I.F. Tretyakov, E.A. Trusova, V.T. Popov, D.I. Slovetsk, Neftechemia 31 (1991) 236.
[12] K. Lozano, E.V. Barrera, J. Appl. Polym. Sci. 79 (2001) 125.
[13] H.M. Cheng, Q.H. Yang, C. Liu, Carbon 39 (2001) 1447.
[14] G. Tibbetts, G.P. Meisner, C.H. Olk, Carbon 39 (2001) 2291.
[15] A.D. Lueking, R.T. Yang, N.M. Rodriguez, R.T.K. Baker, Langmuir 20 (2004) 714.
[16] J.R. Rostrup-Nielsen, J. Catal. 33 (1974) 184.
[17] R.T.K. Baker, Carbon 27 (1989) 315.
[18] J.C. Rodriguez, E. Romeo, J.L.G. Fierro, J. Santamaría, A. Monzón, Catal. Today 37 (1997) 255.
[19] J.I. Villacampa, C. Royo, E. Romeo, J.A. Montoya, P. Del Angel, A. Monzon, Appl. Catal. A 252 (2003) 363.
[20] C. Guimon, A. Auroux, E. Romero, A. Monzon, Appl. Catal. A 251 (2003) 199.
[21] N.M. Rodriguez, J. Mater. Res. 8 (1993) 3233.
[22] G.A. Jablonski, F.W.A.H. Geurts, A. Sacco Jr., Carbon 19 (1992) 99.
[23] V. Ivanov, J.B. Nagy, P. Lambin, A. Lucas, X.B. Zhang, X.F. Zhang, D. Bernaerts, G. Van Tendeloo, S. Amelinckx, J. Van Landuyt, Chem. Phys. Lett. 223 (1994) 329.
[24] P. Wang, E. Tanabe, K. Ito, J. Jia, H. Morioka, T. Shishido, K. Takehira, Appl. Catal. A 231 (2002) 35.
[25] S. Takenaka, Y. Shigeta, E. Tanabe, K.J. Otsuka, J. Catal. 220 (2002) 468.
[26] J. Jia, Y. Wang, E. Tanabe, T. Shishido, K. Takehira, Microporous Mesoporous Mater. 57 (2003) 283.
[27] M.S. Kim, N.M. Rodriguez, R.T.K. Baker, J. Catal. 131 (1991) 60.

[28] L.B. Avdeeva, O.V. Goncharova, D.I. Kochubey, V.I. Zaikovskii, L.M. Plyasova, B.N. Novgorodov, Sh.K. Shaikhutdinov, Appl. Catal. A 141 (1996) 117.
[29] Y. Li, J. Chen, L. Chang, Y. Qin, J. Catal. 178 (1998) 76.
[30] V.V. Chesnokov, V.I. Zaikovskii, R.A. Buyanov, J. Mol. Catal. A 158 (2000) 267.
[31] H. Wang, R.T.J. Baker, Phys. Chem. 108 (2004) 20273.
[32] J.I. Villacampa, N. Latorre, E. Romeo, C. Royo, A. Monzón, J.A. Montoya, in: Proceedings of the XIX Simposio Iberoamericano de Catálisis, Mérida, Yucatán, México, 5–11 September, 2004.
[33] F. Cavani, F. Trifiro, A. Vaccari, Catal. Today 11 (1991) 173.
[34] M. Monthioux, L. Noé, L. Dussault, J.C. Dupin, N. Latorre, T. Ubieto, E. Romeo, C. Royo, A. Monzón, C. Guimon, J. Phys. Chem. B (2007), submitted for publication.
[35] V. Rives (Ed.), Layered Double Hydroxides: Present and Future, Nova Science Publishers, New York, 2001.
[36] Y. Zhao, F. Li, R. Zhang, D.G. Evans, X. Duan, Chem. Mater. 14 (2002) 4286.
[37] J.H. Scofield, J. Electron. Spectrosc. Relat. Phenom. 8 (1976) 129.
[38] S. Casenave, H. Martinez, C. Guimon, A. Auroux, V. Hulea, A. Cordoneanu, E. Dumitriu, Thermochim. Acta 379 (2001) 85.
[39] G. Fierro, M. Lo Jacono, M. Inversi, P. Porta, F. Cioci, R. Lavecchia, Appl. Catal. A 137 (1996) 327.
[40] K.C. Khulbe, R.S. Mann, Catal. Rev. Sci. Eng. 24 (1982) 311.
[41] M. Ferrandon, E. Björnbom, J. Catal. 200 (2001) 148.
[42] R. Brown, M.E. Cooper, D.A. Whan, Appl. Catal. 3 (1982) 177.
[43] V.R. Choudary, A.M. Rajputa, B. Prabhakar, J. Catal. 13 (1993) 326.
[44] J.A. Peña, J. Herguido, C. Guimon, A. Monzón, J. Santamaría, J. Catal. 159 (1996) 313.
[45] A. Monzon, E. Romeo, C. Royo, R. Trujillano, F.M. Labajos, V. Rives, Appl. Catal. A Gen. 185 (1999) 53.
[46] J.C. Rodriguez, A.J. Marchi, A. Borgna, A. Monzon, J. Catal. 171 (1997) 268.
[47] D. Chen, K.O. Christensen, E. Ochoa-Fernández, Z. Yu, B. Tøtdal, N. Latorre, A. Monzón, A. Holmen, J. Catal. 229 (2005) 82.
[48] G.G. Kuvshinov, Yu.I. Mogilnykh, D.G. Kuvshinov, V.I. Zaikovskii, L.B. Avdeeva, Carbon 36 (1998) 87.
[49] M.A. Ermakova, D.Yu. Ermakov, L.M. Plyasova, G.G. Kuvshinov, Catal. Lett. 62 (1999) 93.
[50] G.G. Kuvshinov, D.G. Kuvshinov, A.M. Glushenkov, Chem. Sustain. Devel. 1 (2003) 135.
[51] T.V. Reshetenko, L.B. Avdeeva, Z.R. Ismagilov, A.L. Chuvilin, Appl. Catal. A 247 (2003) 51.
[52] Y. Nishiyama, Y. Tamai, J. Catal. 33 (1974) 98.
[53] A. Monzón, N. Latorre, T. Ubieto, C. Royo, E. Romeo, J.I. Villacampa, L. Dussault, J.C. Dupin, C. Guimon, M. Monthioux, Catal. Today 116 (2006) 264.
[54] M. Pérez-Cabero, E. Romeo, C. Royo, A. Monzón, A. Guerrero-Ruiz, I. Rodríguez-Ramos, J. Catal. 224 (2004) 197.
[55] A. Monzón, N. Latorre, T. Ubieto, A. Valera, E. Romeo, C. Royo, J.I. Villacampa, in: Proceedings of the AICHE 2005 Annual Meeting, Cincinnati OH (E.E.U.U.), October 2005. Ref. meeting del AIChE 2005 y Congreso de desactivacion de 2006.
[56] A. Monzón, N. Latorre, T. Ubieto, A. Valera, E. Romeo, C. Royo, J.I. Villacampa, in: Proceedings of the 10th Symposium on Catalyst Deactivation, Berlín (Alemania), February 2006.
[57] J.W. Snoeck, G.F. Froment, M. Fowles, J. Catal. 169 (1997) 240.
[58] T.V. Reshetenko, L.B. Avdeeva, Z.R. Ismagilov, V.V. Pushkarev, S.V. Cherepanova, A.L. Chuvilin, V.A. Likholobov, Carbon 41 (2003) 1605.
[59] S.K. Doorn, L. Zheng, M.J. O'Connel, Y. Zhu, S. Huang, J. Liu, J. Phys. Chem. 109 (2005) 3751.
[60] F. Tuinstra, J.L. Koenig, J. Chem. Phys. 53 (1970) 1126.
[61] Y. Wang, D.C. Alsmeyer, R.L. McCreery, Chem. Mater. 2 (1990) 557.
[62] T. Jawhari, A. Roid, J. Casado, Carbon 33 (1995) 1561.